Received: 00 Month 0000 | Revised: 00 Month 0000 | Accepted: 00 Month 0000

DOI: xxx/xxxx

REVIEW PAPER

Analysis of the sound sources of lean premixed methane-air flames

Sohel Herff*[1] | Konrad Pausch[1] | Matthias Meinke[2,3] | Wolfgang Schröder[2,3]

[1]Jülich Supercomputing Centre, Forschungszentrum Jülich GmbH, Wilhelm-Johnen-Str., Jülich 52425, Germany

[2]Institute of Aerodynamics and Chair of Fluid Mechanics, RWTH Aachen University, Wüllnerstraße 5a, Aachen 52062, Germany

[3]JARA Center for Simulation and Data Science, RWTH Aachen University, Seffenter Weg 23, Aachen 52074, Germany

Correspondence
*Email: s.herff@aia.rwth-aachen.de

Summary

Two investigations on the sound generation mechanisms of lean methane-air flames are reviewed and linked. A two-step approach is used for the analysis. First, the compressible conservation equations are solved in a large-eddy simulation formulation to compute the acoustic source terms of the reacting fluid. Second, the acoustic source terms are used in computational aeroacoustics simulations to determine the acoustic field by solving the acoustic perturbation equations. To identify the contributions of the different source terms to the overall sound emission of the flames different source term formulations are considered in the computational aeroacoustics simulations. The results of various flames of increasing complexity are shown: Harmonically excited laminar flames, a turbulent jet flame, and an unconfined and a confined swirl flame. The results show that in general the heat release source alone does not determine the acoustic emission of the flame. Only the acoustic emission of the unconfined swirl flame could be computed by the heat release source. To accurately predict the phase and the amplitude of the sound emission of the other flames the acceleration of density gradients occurring at the flame front must be included in the considered set of source terms.

KEYWORDS:
Thermoacoustics, Combustion Noise, Combustion Instabilities, Methane-Air Flames

1 | INTRODUCTION

Combustion instabilities cause high pressure fluctuations in the combustion chamber which can lead to a suboptimal operation or damage the burner assembly [29]. They are usually caused by a closed feedback loop of the flow-flame-acoustic interactions which are often characterized by the acoustic modes of the geometry of the combustion facility. Recent findings show that combustion systems can also be intrinsically unstable [2, 22]. A fundamental understanding of the combustion noise generation mechanisms is necessary to predict and prevent combustion instabilities.

It is common to distinguish between direct and indirect combustion noise [49]. Direct combustion noise originates in the flame front and indirect combustion noise is caused by the acceleration of entropy inhomogeneities [1, 30]. In the current paper, the sound generation mechanisms of direct combustion noise are considered. To avoid combustion instabilities in the early design stages of a combustor low-order models are required. Such models need to include the relevant sound generation mechanisms to predict the correct phase and amplitude of the instabilities. It is common to assume that the fluctuation of the heat release of the flame is the dominant source of sound in the combustion process. Using this assumption an unstable feedback loop occurs if pressure and heat release oscillations are in phase, which is known as the Rayleigh stability criterion [9, 39, 42]. The Rayleigh criterion was used successfully in numerous studies to predict combustion instabilities. However, in some studies the

consideration of the heat release fluctuations as the only source of sound failed to reproduce all the details of the frequency spectrum of combustion noise, e.g., in Bui et al. [6, 7].

To investigate the contributions of the thermoacoustic sound sources various methane-air flames were investigated in Pausch et al. [38] and [36]. A hybrid approach was applied. First, the compressible conservation equations were solved in a large-eddy simulation (LES) formulation and then the noise generation was computed by computational aeroacoustics (CAA) simulations which are based on the acoustic perturbation equations (APE) [12]. The CAA method was applied to analyze the sound emission of different source term formulations which allowed to identify the phase and amplitude relationship of the sound emission of all sound source mechanisms. In the current paper, the major findings of these studies are reviewed and linked. The noise source phase and amplitude relationship is shown for lean-premixed methane-air flames with increasing complexity. First, the sound emission of acoustically excited laminar jet flames is considered. Then, the relevance of the results is demonstrated for a turbulent jet flame. Finally, the analysis is extended for turbulent swirl flames, which have a high industrial relevance, under unconfined and confined operating conditions. All simulations are highly resolved to ensure a high quality of the computed acoustic sources.

The paper, which is based on recently published results, has the following structure. The numerical methods are briefly explained in section 2 before the investigated setups and the source analysis are explained in section 3. Then, the results are analyzed in section 4. Finally, the conclusions are summarized in section 5.

2 | NUMERICAL METHODS

This chapter was published in Flow Turb. Combust., Vol. 103, Pausch et al., "Noise sources of lean premixed flames", 773–796, Copyright Springer (2019) [38]. As stated before, the computational approach is based on a hybrid formulation. First, the conservation equations for a reacting compressible flow are solved in a combustion simulation explained in section 2.1. The solution samples from this simulation are used to compute the time-averaged flow field and the source terms, i.e, for each solution sample of the combustion simulation a source sample is written to disk. The mean flow field and the source samples are the input for the second step, i.e., the subsequent acoustics simulation, which is described in section 2.2. In previous studies, e.g. by Bui et al. [6, 7], a Low-Mach-number simulation was performed for the combustion field in the first step. The acoustic mode was filtered from the combustion simulation and an acoustic analogy formulation was used in the second step. The benefit is a significant overall reduction of computational effort compared to a compressible combustion simulation. However, due to the one-way coupling it is presumed that the flame is perturbed only by hydrodynamic and not acoustic disturbances. The compressible flow model of the current study offers two main advantages. First, the effect of the acoustic-flame interaction is naturally preserved. Second, it allows a CAA validation by comparing the pressure signal from the compressible combustion simulation with that of the acoustics simulation as done in section 4.1.1. The second step of the approach also allows the decomposition of the CAA pressure signal into the contributions of the various sound sources, which are given by the APE formulation presented in section 2.2.

2.1 | Combustion simulation

In the first step of the hybrid approach, the three-dimensional unsteady compressible Navier-Stokes equations are solved using the combined G-equation progress variable modeling approach by Moureau et al. [33] to compute the lean premixed flames. That is, a finite-volume solver is used to solve the conservation equations and a level-set solver is used to track the position of the flame front. For details on the numerical approach to solve the governing equations of the reacting flow, i.e., of the flow field and the combustion field, the reader is referred to, e.g., Herff et al. [21]. The subgrid scale terms arising from the implicit filtering of the governing equations are set to zero, i.e., the dissipative effects of the non-resolved scales are modeled by the numerical dissipation, which is known as MILES approach [3].

The equations are discretized using a strictly conservative finite-volume discretization with a second-order accurate modified low-dissipation AUSM scheme [17, 18, 19] for the convective terms and second-order accurate central differences for the viscous terms. A third-order total-variation diminishing (TVD) Runge-Kutta scheme is used for the integration in time. A conservative cut-cell technique captures arbitrary embedded boundaries [45, 46]. This solver has extensively been validated in [43] by comparing distributions of turbulent kinetic energy, heat release spectra, turbulent mass consumption, cold flow statistics, and boundary layer characteristics against experimental data for a slot flame. The present computations use a static mesh for the finite-volume solver and a solution adaptive mesh for the level-set solver. The finite-volume solver and the level-set solver are

coupled using a joint hierarchical mesh. A fully automated dynamic load balancing method was adapted for the coupled finite-volume and level-set solvers. For details on the solver coupling and the dynamic load balancing method the reader is referred to [21].

2.2 | Acoustics simulation

In the second step, the acoustic field is determined by solving the acoustic perturbation equations (APE) [12]. The left-hand side of the APE corresponds to the acoustically filtered linearized Navier-Stokes equations extended for a non-uniform mean flow field and describes the acoustic wave propagation into the far field. The right-hand side of the APE consists of the source terms which determine the acoustic emission. The variables are decomposed into a temporal mean $\bar{\cdot}$ and fluctuating component $\cdot'$, i.e., for a variable Φ the decomposition yields $\Phi = \bar{\Phi} + \Phi'$. In the APE-4 formulation [12] the perturbation density is eliminated by combining the energy and continuity equation

$$\frac{\partial p^a}{\partial t} + \overline{c^2}\boldsymbol{\nabla}\cdot\left(\overline{\rho}\boldsymbol{v}^a + \overline{\boldsymbol{v}}\frac{p^a}{\overline{c^2}}\right) = \overline{c^2}q_c + q_e \underbrace{- \overline{c^2}\boldsymbol{\nabla}\cdot\left(\overline{\boldsymbol{v}}\rho_e\right)}_{q_{c\&e}} \tag{1}$$

$$\frac{\partial \boldsymbol{v}^a}{\partial t} + \boldsymbol{\nabla}\left(\overline{\boldsymbol{v}}\cdot\boldsymbol{v}^a\right) + \boldsymbol{\nabla}\left(\frac{p^a}{\overline{\rho}}\right) = \boldsymbol{q_m}. \tag{2}$$

This results in an additional source term $q_{c\&e}$ besides the continuity source term q_c, the energy source term q_e, and the momentum source term $\boldsymbol{q_m}$. Due to the extension to a non-uniform mean flow field, convection and refraction effects are taken into account by the left-hand side operator. The system of equations is solved for the perturbation pressure p^a and the perturbation velocity $\boldsymbol{v}^a$. The results from the combustion simulation are used to determine the mean flow quantities, i.e., the mean density $\bar{\rho}$, the mean velocity $\bar{\boldsymbol{v}}$, and the mean squared speed of sound $\bar{c^2}$, and the sources

$$q_c = -\boldsymbol{\nabla}\cdot\left(\rho'\boldsymbol{v}'\right)' \tag{3}$$

$$q_e = \frac{\partial p'}{\partial t} - \overline{c^2}\frac{\partial \rho'}{\partial t} \tag{4}$$

$$\boldsymbol{q_m} = (\boldsymbol{\omega}\times\boldsymbol{v})' - \boldsymbol{\nabla}k' + \underbrace{\boldsymbol{\nabla}\left(\frac{p'}{\overline{\rho}}\right) - \left(\frac{\boldsymbol{\nabla}p}{\rho}\right)'}_{q_{m,p}} + \underbrace{\left(\frac{\boldsymbol{\nabla}\cdot\underline{\boldsymbol{\tau}}}{\rho}\right)'}_{neglected}, \tag{5}$$

which further include the vorticity $\boldsymbol{\omega}$, the turbulent kinetic energy k, and the stress tensor $\underline{\boldsymbol{\tau}}$. Since the APE-4 system is derived by rewriting the governing equations such that the left-hand side corresponds to the APE-1 operator [12], the source terms on the right-hand side are not filtered and also support vorticity modes. However, unlike the linearized Euler equations the APE system is still stable [12]. Outside the noise source region, which will be denoted in the following as source region, the right-hand side vanishes and the fluctuations in pressure and velocity computed by the APE operator contain only the acoustic mode. The acoustic perturbation equations are discretized in space by a 9-point 6th-order dispersion-relation preserving summation by parts scheme (SBP-DRP) [25]. The temporal integration is done by an alternating 5-6 stage low-dispersion low-dissipation Runge-Kutta scheme (LDDRK) [23]. The acoustic source terms are determined by temporally interpolating the LES results, which are sampled at a relatively high frequency. For details on the time interpolation scheme, the reader is referred to [14].
This hybrid method for the acoustic analysis was successfully applied to turbulent premixed slot [44] and diffusion flames [6].

3 | NUMERICAL CONFIGURATIONS

The discussion focuses on the analysis of the sound source mechanisms of laminar and turbulent flames described by the conservation equations. The generic setup of the laminar flames in section 3.1 allows the analysis of the source terms over a range of operating parameters without broadband spectral fluctuations. This enables a straightforward interpretation of the mechanisms of noise generation since no noisy broadband signal of a turbulent flame exists. Further, a direct comparison of the pressure signals from the combustion simulation and the acoustics simulation to validate the CAA approach is possible. The relation

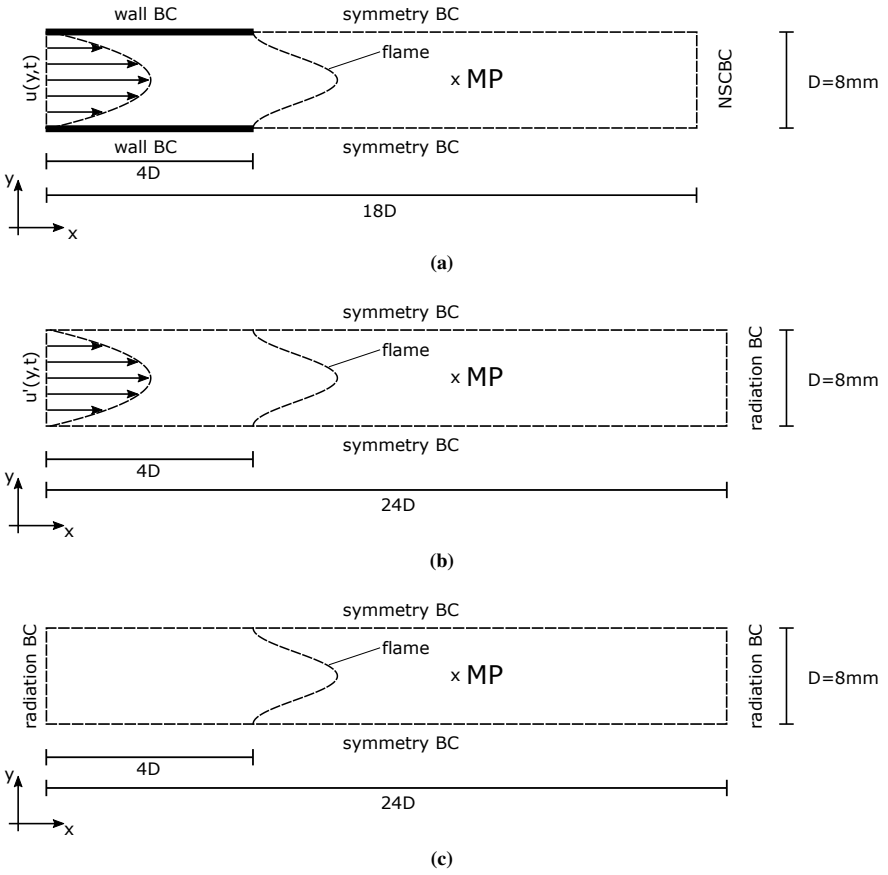

FIGURE 1 Schematics (not to scale) of the computational setups of the combustion simulation (a) and the CAA simulations (b),(c) of the laminar flames. The pressure signal is recorded at the monitoring point (MP) on the centerline 3D downstream of the flame base, which is in the region of burnt gas for all investigated cases [38].

of the fundamental findings for the generic laminar flame to that of a turbulent jet flame is demonstrated in section 4.2. The experimental setup of the turbulent jet flame is described in section 3.2 and in section 4.2 the approach is validated by experimental results. The swirl burner configuration in section 3.3 is used to extend the analysis of the sound source mechanisms of laminar and turbulent jet flames to unconfined and confined swirl flames. The chapters 3.1, 3.2, and 3.4 were published in Flow Turb. Combust., Vol. 103, Pausch et al., "Noise sources of lean premixed flames", 773–796, Copyright Springer (2019) [38]. The chapter 3.3 was published in J. Sound Vib., Vol. 475, Pausch et al., "Noise sources of an unconfined and a confined swirl burner", 115293, Copyright Elsevier (2020) [36].

3.1 | Laminar flames

A sketch of the computational setups of the laminar flames is given in figure 1 . The domain of the combustion simulation is sketched in figure 1 (a). Acoustic simulations are performed with two different computational setups that are shown in figure 1 (b) and figure 1 (c). Note that radiation boundary conditions [53] are defined at the inlet and outlet in figure 1 (c) such that the pure acoustic emission of the flame can be analyzed. The total length of the domain is 18D for the combustion simulation (figure 1 (a)) and 24D for the acoustic simulation (figures 1 (b),(c)), where $D = 8\text{mm}$ is the domain width. For the combustion and the acoustic simulations, the domain inlet is located 4D upstream of the flame base. In all laminar combustion simulations, a temporally oscillating parabolic inlet velocity is prescribed as

$$u(y,t) = u_p(y) \cdot (1 + a \cdot \sin(2\pi f t)) \,. \tag{6}$$

Combustion and acoustic simulations are performed at varying inlet velocity excitation amplitudes a and frequencies f as listed in table 1 . The fresh gas enters the domain at temperature $T_0 = 300\text{K}$ and pressure $p_0 = 1\text{bar}$. The Reynolds number based on

T_b/T_u	a	f[Hz]	$u_{p,max}$[m/s]	$Re(u_{bulk})$
6.9	0.1, 0.3	50, 100, 200, 400	1.6	569

TABLE 1 Parameters of the laminar flame configurations

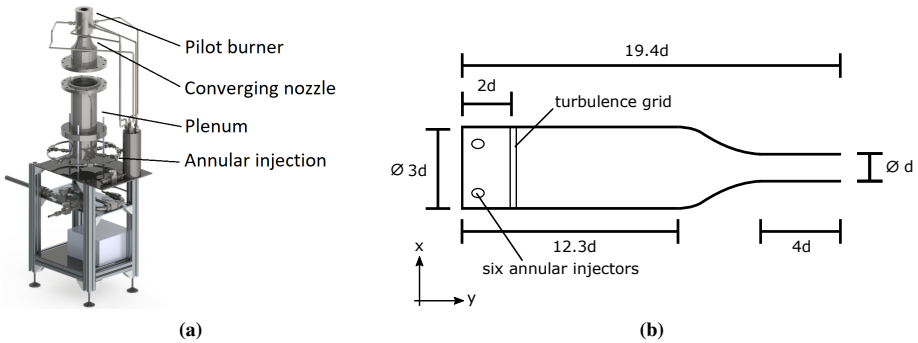

FIGURE 2 Schematics (not to scale) of the experimental burner configuration of the turbulent jet flame by Nawroth and Paschereit [35, 38].

the averaged inlet velocity is $Re = 569$. The current results are from computations with a temperature ratio of the burnt (b) and unburnt (u) gas of $T_b/T_u = 6.9$ which corresponds to a realistic methane-air mixture at an equivalence ratio of $\phi = 0.9$ [34]. Note that in Pausch et al. [38] computations with a second temperature ratio of $T_b/T_u = 2.3$ were performed to investigate the effect of the temperature gradient at the flame surface on the acoustic sources.

No-slip wall boundary conditions are used at the lateral faces of the domain upstream of the flame base. Symmetry boundary conditions are used at the lateral faces of the domain downstream of the flame base. To bypass sound-waves at the domain outlet, the characteristic boundary conditions by Poinsot and Lele [40] are used.

For the acoustic simulations two computational setups are used. Both apply symmetry conditions to the lateral faces of the domain and a radiation boundary condition [53] at the domain outlet to ensure non-reflectivity. At the domain inlet, in the first setup, see figure 1 (b), the oscillating parabolic profile of the combustion simulation is prescribed in perturbation form

$$u'(y,t) = u_p(y) \cdot a \cdot \sin(2\pi f t). \tag{7}$$

This allows the validation of the CAA method in section 4.1.1 by comparing the pressure signals from the combustion and the acoustic simulations. It ensures that the CAA solution of the APE-4 system accurately reproduces the pressure signal from the compressible combustion simulation. The second setup illustrated in figure 1 (c) contains a radiation boundary condition at the inlet to analyze the acoustic emission of the flame without any reflections from the domain boundaries. This domain is used to investigate the flame's sound generation mechanisms in section 4.1.2. Note that the same data from the combustion simulation with velocity forcing at the inlet is used. All signals are recorded at a monitoring point on the centerline at $x = 3$D downstream of the flame base.

3.2 | Turbulent jet flame

Figure 2 schematically shows the turbulent jet flame facility from TU Berlin [35]. A lean mixture of methane and air enters the burner plenum through six annular injection drillings and exits the burner after a converging nozzle. The outlet diameter is $d = 0.035$m. The Reynolds number based on the flow conditions at the burner outlet is $Re_d = 10,000$. To ensure a stable operation at an equivalence ratio of $\phi = 0.7$, the turbulent flame is piloted at the outlet by an annular gap flame with the same equivalence ratio. The acoustic pressure is measured at a microphone position $r = 30$d, i.e., on the burner outlet plane at a distance of 1.05m from the centerline. The experiments were done by Nawroth and Paschereit in an anechoic environment [35]. The large-eddy simulation (LES) domain in figure 3 (a) contains $87 \cdot 10^6$ grid points. To accurately reproduce the experimental turbulent flow field, the full burner plenum with annular injection of the methane-air mixture is included. The turbulence grid,

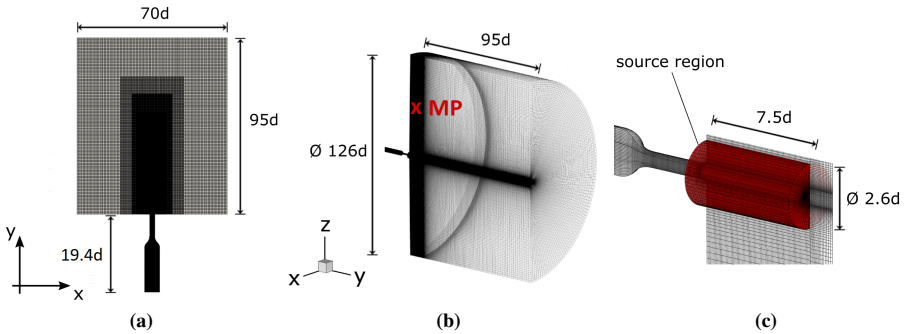

FIGURE 3 LES domain (a) and CAA domain (b) of the turbulent jet flame configuration including the source region colored in red (c) [38].

which is shown in figure 2 (b), is included in the computational domain. It consists of a checkerboard structure with rods having a rectangular cross section and it blocks approximately 18% of the plenum cross section. Local refinement in the burner plenum and the jet region leads to an isotropic cell spacing of $\Delta_{cell} = 0.0187$d. At the outflow of the domain, the characteristic boundary conditions by Poinsot and Lele [40] are used. Inviscid wall boundary conditions with sponge layers are imposed on the lateral faces of the domain. No-slip adiabatic boundary conditions are applied to the burner walls.
Figure 3 (b) shows the CAA domain. The structured mesh consists of $63 \cdot 10^6$ cells. Inviscid wall boundary conditions are applied at the burner walls. At the far-field boundaries, the radiation boundary condition by Tam and Webb is used [53]. In the source region shown in figure 3 (c), the source terms on the right-hand side of the APE-4 system in equations 1 and 2 are computed on the LES grid and interpolated onto the CAA grid based on an inversed distance weighting of the nearest neighbors for the subsequent acoustic computation. The source region in the CAA simulations is a cylindrical domain that extends from 0.5d upstream of the burner outlet to 7.5d downstream of the burner outlet with a diameter of 2.6d. Only the noise generated in the flame region is computed by the CAA simulations, i.e., the noise generated by the plenum flow is neglected within the CAA simulations. Buffer zones that damp the source terms are used at the boundaries of the source region to avoid spurious noise generation. It was found that enlarging the source region by 50% in the radial and axial direction shows no significant change in the acoustic results. Therefore, the current source region is considered large enough to capture the relevant noise generating flow features.

3.3 | Swirl Flames

The confined swirl burner investigated in the current study corresponds to the experimental configuration by Moeck et al. [32]. The geometry shown in figure 4 was kindly provided by EM2C [4, 32]. A lean premix of methane and air enters the plenum at an equivalence ratio of $\phi = 0.67$. Downstream of a converging nozzle the flow passes through a 9-blade radial swirler. Bourgouin et al. [4] found for this particular burner that small geometrical deviations of the actual swirler from the drawing, which occur due to manufacturing limitations, impact the swirl number and thus the flow field in the combustion chamber. Therefore, the current study uses the actual manufactured swirler geometry provided by EM2C [4]. The resulting swirl number is $S = 0.73$. The Reynolds number based on the diameter of the injection tube downstream of the swirler $D_{SB} = 12$mm is $Re_{D,SB} = 8800$. The flame is symmetrically confined by the cylindrical combustion chamber which has a diameter of $4.2D_{SB}$ and a length of $25D_{SB}$.
The LES domain is shown in figure 5 (a). In the experiments, the premix enters the plenum through two diametrically opposed injectors [32]. Therefore, an arrangement consisting of a honeycomb and two grids is used to straighten the flow upstream of the converging nozzle. Note that this arrangement is not part of the LES. Instead, the LES domain inlet is located just upstream of the converging nozzle and non-reflecting Navier-Stokes characteristic boundary conditions (NSCBC) [40] with a parabolic inflow velocity profile are imposed. Since no detailed information on the experimental temperature distribution of the burner walls is available, an adiabatic no-slip boundary condition is assumed in the LES. Note that this is a possible source for some disagreement between numerical and experimental results, since it is known that the burner wall temperature impacts the gas temperature and thus, the flame dynamics and the acoustic field [10, 28, 31].

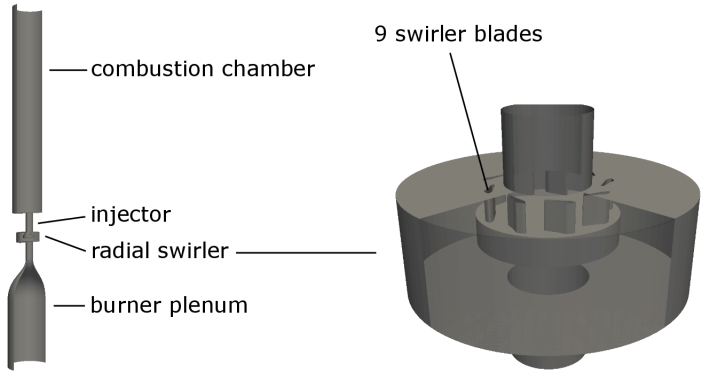

(a)

FIGURE 4 Three-dimensional model of the burner geometry of the swirl flame configuration by EM2C [36].

The CAA domain is shown in figure 5 (b). In the LES and the CAA domain an additional volume is attached to the combustion chamber to mimic the experimental boundary conditions. To ensure non-reflectivity, the LES uses the NSCBC and the CAA the radiation boundary conditions [53]. Due to the structured grid topology in the CAA solver, the CAA domain does not contain the injector with swirling unit. An acoustic wall boundary condition is imposed at the injector exit plane, i.e., in the beginning of the combustion chamber. At the combustor walls, slip-wall boundary conditions are imposed. For the source analysis of the confined setup, the pressure is recorded at a monitoring position located on the centerline $16\mathrm{D_{SB}}$ downstream of the injector exit plane. In addition to the confined setup, the same burner is investigated also in an unconfined configuration, i.e., without combustion chamber walls. This allows to analyze the radiation characteristics and the noise sources without acoustic feedback from the combustion chamber geometry. The pressure is recorded at $(y, r) = (2.5\mathrm{D_{SB}}, 15\mathrm{D_{SB}})$.

The LES mesh is shown in figure 6 (a). It is a Cartesian grid with approximately $200 \cdot 10^6$ cells for the confined burner and approximately $350 \cdot 10^6$ cells for the unconfined burner. Hierarchical refinement allows to accurately resolve large gradients in the flow which occur, e.g., in the swirler. This swirler is resolved by approximately 25 cells along the swirler blade. The curvilinear mesh used in the CAA simulations is sketched in figure 6 (b). The source region inside the combustion chamber is colored in red. It is a cylindrical domain with a radius of $2\mathrm{D_{SB}}$ that extends from the injector exit plane to a position $7\mathrm{D_{SB}}$ downstream of it. Buffer zones that damp the source terms are used at the boundaries of the source region to avoid spurious noise generation. To keep interpolation errors inside the source region low, the grid points of the inner Cartesian region coincide with the LES grid points. The CAA mesh includes approximately $90 \cdot 10^6$ cells for the confined and $200 \cdot 10^6$ cells for the unconfined configuration.

3.4 | Thermoacoustic source analysis

For the thermoacoustic analysis, the energy source equation 4 is reformulated [15]

$$\begin{aligned} q_e &= \frac{\partial p'}{\partial t} - \overline{c^2}\frac{\partial \rho'}{\partial t} \\ &= \underbrace{\left(\frac{\mathrm{D}p}{\mathrm{D}t} - c^2\frac{\mathrm{D}\rho}{\mathrm{D}t}\right)'}_{q_{e,I}} + \underbrace{\left(\left(c^2\right)'\frac{\partial \rho}{\partial t}\right)'}_{q_{e,II}} + \underbrace{\left(\boldsymbol{v}\cdot\left(c^2\boldsymbol{\nabla}\rho - \boldsymbol{\nabla}p\right)\right)'}_{q_{e,III}}. \end{aligned} \tag{8}$$

The substantial pressure-density relation $q_{e,I} = q_{e,h} + q_{e,I,res}$ contains the heat release by chemical reactions $q_{e,h} = (\gamma - 1)\dot{Q}'$ and other source terms from irreversible mechanisms $q_{e,I,res}$ caused by diffusive fluxes [8, 15]. The source term $q_{e,II}$ accounts for local fluctuations in the speed of sound, which are mainly induced by the flame front motion. Using Gibb's fundamental equation of thermodynamics, the last term $q_{e,III}$ is reformulated to evidence the acceleration of entropy inhomogeneities [15]

$$q_{e,III} = -((\gamma - 1)\,\rho T\boldsymbol{v}\cdot\boldsymbol{\nabla}s)', \tag{9}$$

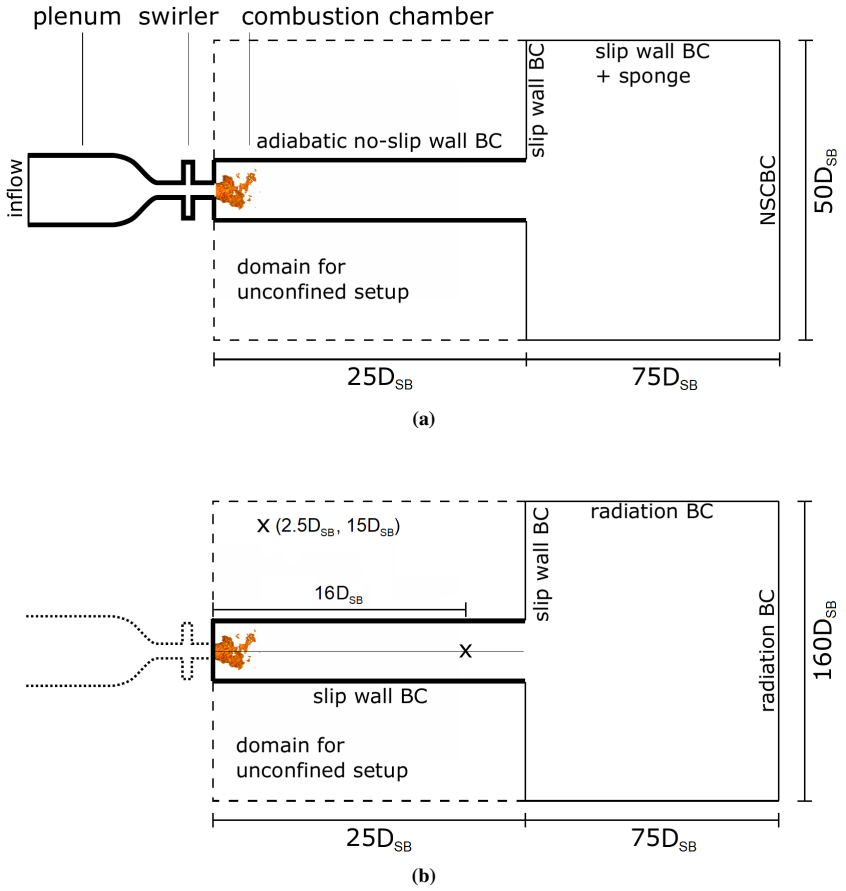

FIGURE 5 Schematics (not to scale) of the computational setups of the LES (a) and the CAA simulations (b) of the swirl flame configuration. The reference length $D_{SB} = 12$mm is the diameter of the injection tube located between the swirler and the combustion chamber [36]. The two monitoring positions in the CAA domain are indicated by the crosses. The first is located $16D_{SB}$ downstream of the injection tube and the second is located at $(y, r) = (2.5D_{SB}, 15D_{SB})$

where γ is the ratio of specific heats and s the mass specific entropy of the particular species k of a total number of N species. In the following, this term $q_{e,III}$ will be denoted entropy noise source. Note that though entropy noise effects related to $q_{e,III}$ are known to cause indirect combustion noise [1, 30], the term $q_{e,III}$ is considered in the current analysis as a physical sound generation mechanism of direct combustion noise, since no mean flow gradient inducing devices such as a nozzle or a turbine are included in the investigated flow domains. Futhermore, the current combustion model assumes a perfectly premixed flame. Hence, the flames under investigation do not produce entropy inhomogeneities from fluctuations in the mixture composition, the associated sound generation of which is discussed in [24, 27, 50]. However, the term is included in the current analysis, since for the setups under investigation the term $\boldsymbol{v} \cdot \boldsymbol{\nabla} s$ is considerable at the flame front, where the entropy gradient is significant, and this flame front is perturbed by velocity fluctuations from the inlet forcing.

The noise generation mechanisms of the flames are investigated by comparing the CAA pressure signals generated by the individual source terms with the CAA pressure signals obtained by using the complete set of source terms of the APE-4 system. The objective is to find the sound mechanisms dominating the overall sound emission in the sense that they reproduce phase and magnitude of the acoustic pressure signal signals with reasonable accuracy and to analyze their phase relationship.

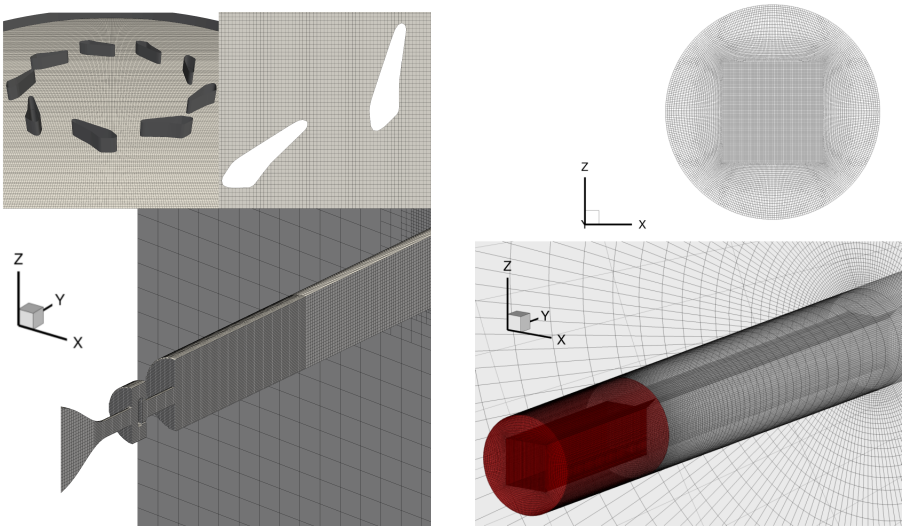

FIGURE 6 Computational meshes of the LES (a) and the CAA simulations (b) of the swirl flame configuration. The top figure of (a) depicts the LES grid in the swirler unit. The bottom of figure (a) displays only every eighth grid point. The top figure of (b) shows every second grid point of a cross section of the source region. The bottom of figure (b) shows every fourth grid point of the CAA mesh of the combustion chamber. The source region is colored in red [36].

4 | RESULTS

The discussion of the results is structured as follows. First, the results of the laminar flame computations are discussed in section 4.1. This includes the comparison of the pressure signal from the CAA simulations using the APE-4 equations including the complete set of source terms with the pressure signal from the compressible combustion simulations in section 4.1.1. In section 4.1.2, the acoustic source terms of the laminar flames are analyzed. Then, the thermoacoustic sources terms of the turbulent jet flame are investigated in section 4.2. Finally, the source terms of the unconfined and the confined swirl flames are analyzed in section 4.3. The chapters 4.1 and 4.2 were published in Flow Turb. Combust., Vol. 103, Pausch et al., "Noise sources of lean premixed flames", 773–796, Copyright Springer (2019) [38]. The chapter 4.3 was published in J. Sound Vib., Vol. 475, Pausch et al., "Noise sources of an unconfined and a confined swirl burner", 115293, Copyright Elsevier (2020) [36].

4.1 | Laminar flames

Figure 7 (a) shows contours of the mean temperature field exemplarily for the case $T_b/T_u = 6.9$, $a = 0.3$, $f = 100$Hz. Note that the wave length of the flame-incident velocity perturbation is larger than the flame length for all investigated cases. The flames respond to the inflow velocity modulation by flame height oscillations indicated by the flame front position for the minimum flame height $L_{f,min}$ and the maximum flame height $L_{f,max}$ in figure 7 (a). The amplitudes of the flame height oscillations $L'_f(f)$ are shown in figure 7 . Except for the case $T_b/T_u = 6.9$, $a = 0.3$, $f = 200$Hz, the flame response generally decreases with increasing excitation frequency. This is in qualitative agreement with theoretical and experimental results from the literature for flames under uniform velocity perturbations [11, 13, 48, 54]. For the temperature ratio $T_b/T_u = 6.9$ and the higher excitation amplitude $a = 0.3$, the strong flame height oscillation at the excitation frequency $f = 200Hz$ is connected to the separation, shedding, and annihilation of a flame pocket during each excitation period which was discussed in more detail in Pausch et al. [38].

4.1.1 | CAA validation

For each set of parameters given in table 1 a CAA simulation using the configuration shown in figure 1 (b) was conducted based on all the source terms of the APE-4 system, i.e., including the full continuity source term in equation 3, the momentum

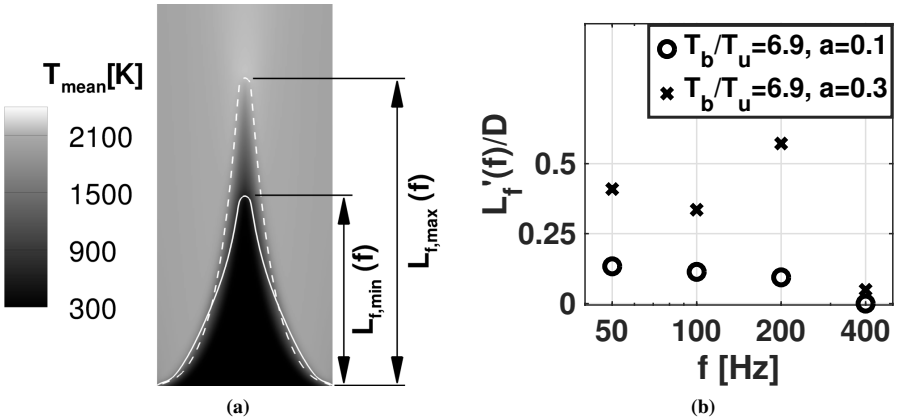

FIGURE 7 (a) Contours of the mean temperature of the laminar flame case $T_b/T_u = 6.9$, $a = 0.3$, $f = 100$Hz. The flame position is indicated by isolines of a constant progress variable $c_s = 0.5$ for the minimum (solid) and maximum (dashed) flame height L_f during the excitation period. (b) Amplitude $L'_f(f)$ of the flame height oscillations of the laminar flames as a function of frequency [38].

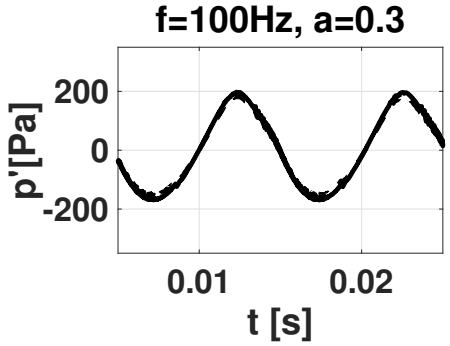

FIGURE 8 Pressure signals from the CAA simulation (dashed line) and the compressible combustion simulation (solid line) of the laminar flame configuration for $T_b/T_u = 6.9$, $a = 0.3$, and $f = 100$Hz [38].

source term in equation 5, where the last term including viscous effects is neglected, and the full energy source term given by equation 8. The results for $T_b/T_u = 6.9$, $a = 0.3$, $f = 100$Hz are shown in figure 8 .

Evidently, the two lines cannot be told apart. Therefore, the sinusoidal pressure signals from both computational methods are in good agreement as to magnitude and phase. Thus, the APE-4 system containing the complete set of source terms convincingly reproduces the combustion noise calculated applying the entire system of conservation equations.

Note that this validation comprises all the source terms of the APE-4 system and not just the heat release source term. The comparison of the pressure signal including all the source terms with the pressure signal obtained just by the heat release fluctuations $q_{e,h} = (\gamma - 1)\dot{Q}'$ is given in figure 9 for the case $T_b/T_u = 6.9, a = 0.3, f = 100$Hz. The figure clearly exhibits that the pressure signal generated by the complete set of source terms, which is, as discussed above, in good agreement with the pressure signal from the compressible flow simulation, is changed in amplitude and shifted in phase if only the heat release fluctuations are considered in the source terms. Similar discrepancies were also found for the remaining cases. To further analyze the effects of the obviously non-negligible remaining source terms, the APE formulation is used to decompose the acoustic pressure signal into the components generated by the individual source terms. The results are comprehensively presented for all the cases in the next section.

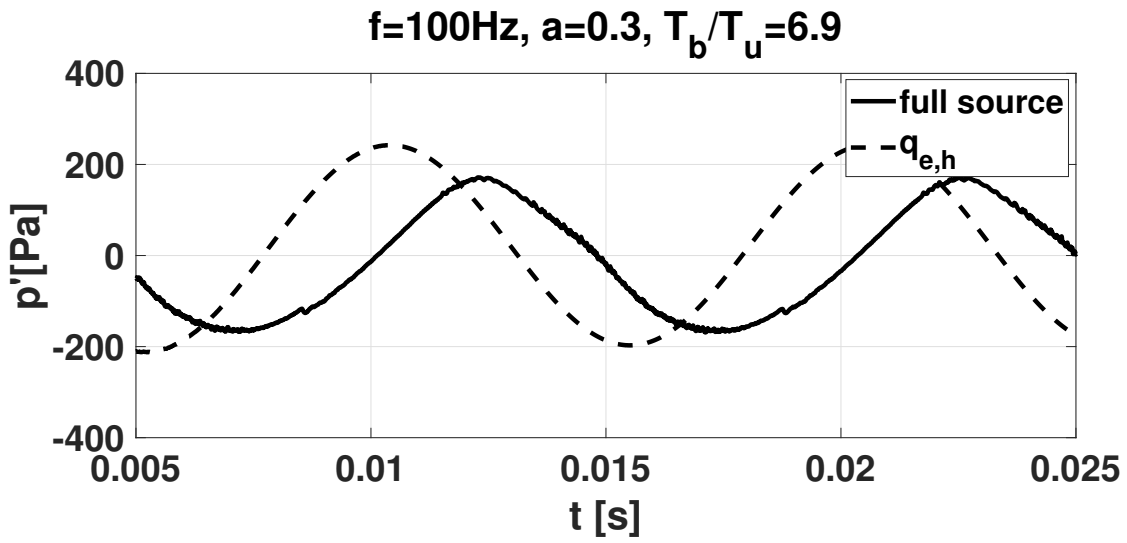

FIGURE 9 Pressure signals from the CAA simulation of the laminar flame configuration based on the complete set of source terms (solid line) and the heat release source term (dashed line) [38].

4.1.2 | Acoustic source analysis of the laminar flames

To analyze the acoustic response mechanisms of the laminar excited flame isolated from reflection effects at the inlet and outlet boundaries, a radiation boundary condition is used in the CAA simulations at the domain inlet. In the following, results from the APE-4 system with a reduced set of source terms are presented first. This reduced set of source terms accurately reproduces the pressure signals calculated with the complete source terms. Then, the source terms of the reduced set are analyzed.

Figure 10 shows the phase and magnitude of the Fourier transformed pressure signals obtained by the source terms $q_{e,I}$, $q_{e,III}$, and $q_{m,p}$ in comparison with the formulation including the complete set of source terms for all parameter sets from table 1 . The term $q_{e,I}$ includes the heat release source term, $q_{e,III}$ is the entropy noise source term, and $q_{m,p}$ is a pressure amplification term. The source terms are given by the first and third term on the right-hand side of equation 8 and the third term on the right-hand side of equation 5. The phases are taken with respect to the phase of the oscillating inflow velocity of the combustion simulation, which differs from the excitation velocity at the flame base due to the reflection of the upstream traveling wave at the inlet boundary of the combustion simulation.

In the range of variation of the parameters the magnitude of the total acoustic flame response increases approximately proportional to the excitation amplitude. The reduced set of source terms predicts phase and magnitude in good agreement with the complete set of source terms. Note that the inclusion of the three sources terms, i.e., $q_{e,I}$, $q_{e,III}$, and $q_{m,p}$, into the CAA computations is necessary to accurately predict the acoustic pressure signal for all investigated configurations. Therefore, they are

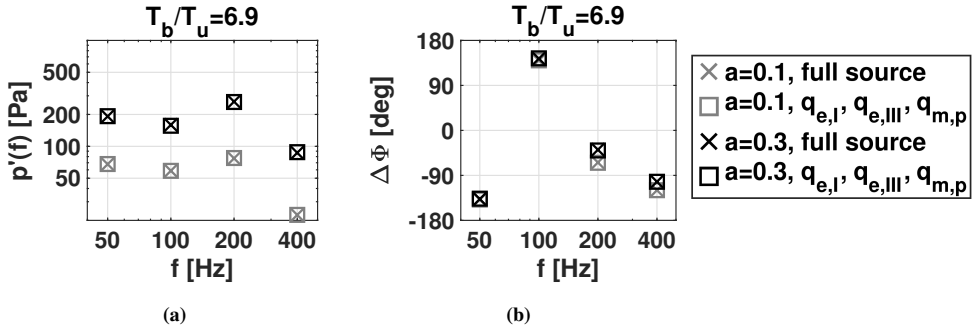

FIGURE 10 Magnitude (a) and phase (b) of the pressure signals of the laminar flame configuration with the complete set of source terms and the signals based on a reduced set of source terms [38].

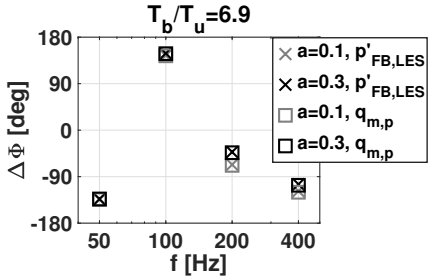

FIGURE 11 Comparison of the phases of the pressure from the compressible combustion simulation of the laminar flame configuration taken at the flame base and the CAA calculated pressure generated on the centerline at $x = 3D$ downstream of the flame base by the source term $q_{m,p}$ [38].

considered the dominant and essential sound source terms that are investigated next.
Unlike the source terms $q_{e,I}$ and $q_{e,III}$, we consider the term $q_{m,p}$ to account for amplification effects of pressure waves at the flame front, since for negligible pressure gradients the term reduces to $q_{m,p} \approx p'\nabla\left(1/\overline{\rho}\right)$. Figure 11 comparatively juxtaposes the phases of the CAA pressure signal generated by $q_{m,p}$, which is recorded on the centerline at $x = 3$D downstream of the flame base, and the pressure at the flame base taken from the combustion simulation described in section 2.1. The retarded time of the sound wave traveling from the flame base to the CAA microphone is negligible compared to the cycle duration. It is evident that the term $q_{m,p}$ generates sound which is in phase with the pressure at the flame. This confirms that $q_{m,p}$ amplifies pressure waves. The term is significant for the investigated setups, since the oscillating inflow velocity generates acoustic waves that are amplified at the flame front.

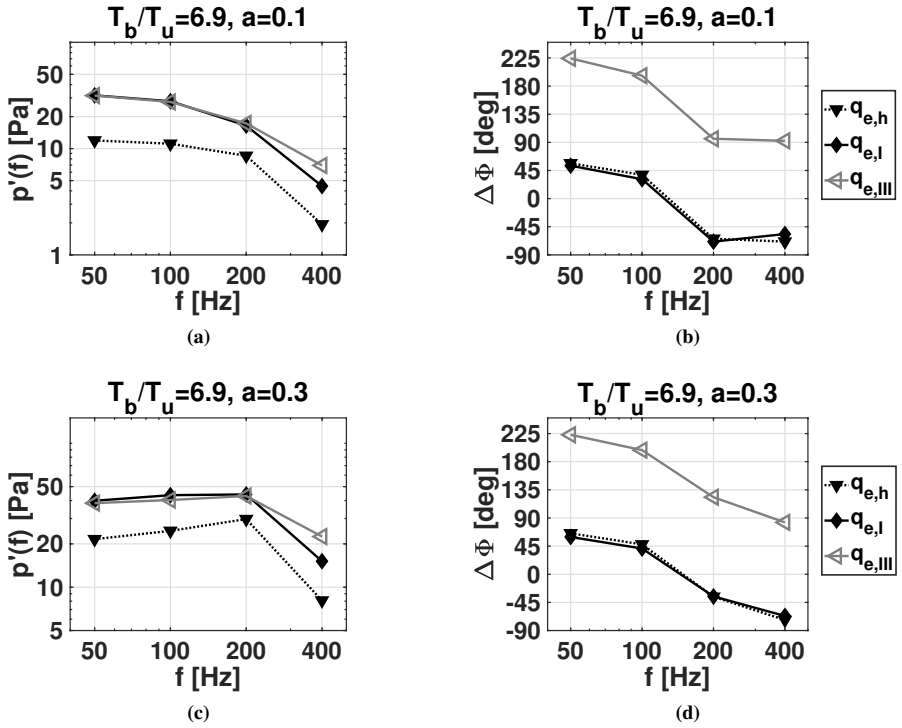

FIGURE 12 Magnitude and phase of the CAA calculated pressure signal of the laminar flame configuration generated by the energy source terms $q_{e,I}$, $q_{e,III}$, and for the temperature ratio $T_b/T_u = 6.9$ and the amplitudes $a = 0.1$ (a),(b) and $a = 0.3$ (c),(d) [38].

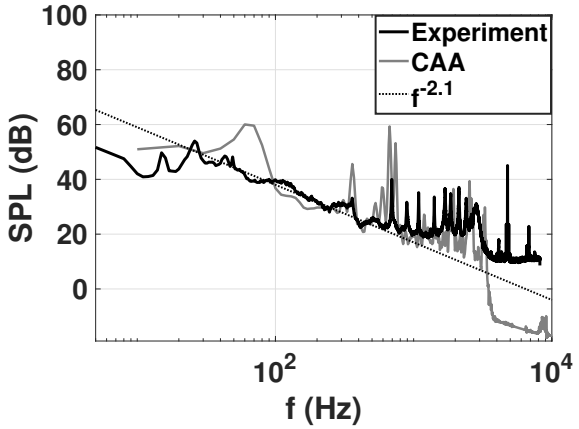

FIGURE 13 Experimental [37] and CAA SPL spectrum [38] of the turbulent jet flame. The full set of acoustic sources is used for the CAA computation.

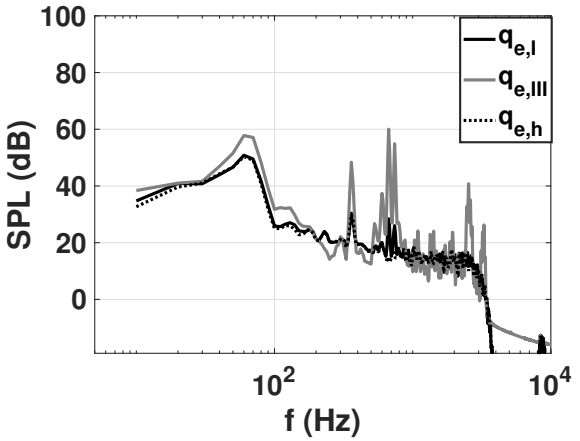

FIGURE 14 Comparison of the noise emission of the turbulent jet flame by the sources $q_{e,I}$, $q_{e,III}$, and $q_{e,h}$ [38].

The contributions of the thermoacoustic subterms $q_{e,I}$, $q_{e,h}$, and $q_{e,III}$ of the energy source term q_e are given in figure 12 . The substantial pressure-density source term $q_{e,I}$ and its heat release subsource term $q_{e,h}$ are highly correlated. Their resulting pressure magnitude spectra are qualitatively similar. The quantitative shift is caused by the contribution of the diffusive mechanisms. Note that both are in phase. The noise generated by $q_{e,III}$ is on the same order as the noise emitted by $q_{e,I}$. However, their phases differ significantly. This leads to a strong phase shift in the signal calculated with the complete set of source terms and emphasizes the importance of this source term for the analysis of thermoacoustic instabilities, since the phase information is crucial for determining the growth rate or decay rate of thermoacoustic modes in a combustor system.

As stated before, we consider the sound from $q_{e,III} = -((\gamma - 1)\,\rho T \boldsymbol{v} \cdot \boldsymbol{\nabla} s)'$ as entropy noise near the flame front. Compared to $q_{e,I}$ its relative contribution, i.e., the contribution against $q_{e,I}$ and $q_{e,h}$, increases for the higher frequencies. This can be explained by the flame response to the inflow excitation. For the higher frequencies the flame response is weaker than for the lower frequencies. This leads to very small flame surface fluctuation amplitudes and as such heat release perturbations at $f = 200$Hz and $f = 400$Hz. Consequently, the heat-release driven noise by $q_{e,I}$ and q_e, h is significantly reduced. Two effects, however, contribute to the sound emission of the entropy noise term. The first effect is connected to the local changes of the entropy gradient $\sim \boldsymbol{v} \cdot \boldsymbol{\nabla} s'$, i.e., the motion of the flame front. The second effect is due to the change in the flow velocity at the flame front $\sim \boldsymbol{v}' \cdot \boldsymbol{\nabla} s$. The latter term contributes to the generation of noise even at high frequencies, when the flame barely responds to the excitation. The latter of which is shown in figure 7 .

4.2 | Acoustic source analysis of a turbulent jet flame

In this section, the acoustic emission of the turbulent premixed jet flame, the computational setup of which is concisely described in section 3.2, is discussed to exemplarily demonstrate the relevance of the noise generating mechanisms observed for the generic laminar flames in section 4.1.2 for this turbulent flame. The acoustic analysis is based on the flow solver presented in section 2.1 which has been validated extensively against experimental data for a slot flame. For the axisymmetric jet flame, a comparison of numerically and experimentally determined flow statistics is shown, e.g., in Herff et al. [20].

Figure 13 comparatively juxtaposes the experimental sound pressure level (SPL) and the CAA calculated spectra based on the formulation with the complete set of source terms. The operating conditions for the jet flame are given in section 3.2. The flame is excited by turbulence leading to a broadband noise spectrum and additionally by acoustic modes which generate noise at several distinct frequencies. A good agreement between the spectra of the CAA prediction and the experimental data by Nawroth and Paschereit [35] is found in the mid frequency range. The spectral decay rate $f^{-2.1}$ is similar to the results reported by Rajaram and Lieuwen [41]. The acoustic modes exciting the jet flame originate from the burner plenum. These modes and their impact on the motion of the jet flame and thus the acoustic emission were analyzed in detail in Herff et al. [20]. An additional peak occurs in the CAA simulation at $f \approx 60$Hz, which is the frequency of the Helmholtz resonance of the burner. This resonance is damped in the experiments due to the interaction of the inlet jets and the plenum flow, which is not included in the LES domain.

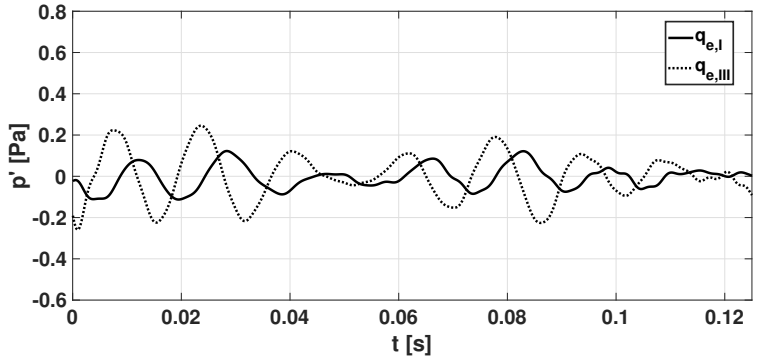

FIGURE 15 Pressure signals of the turbulent jet flame obtained considering the source terms $q_{e,I}$ and $q_{e,III}$ filtered to include only frequency components $f < 300Hz$ [38].

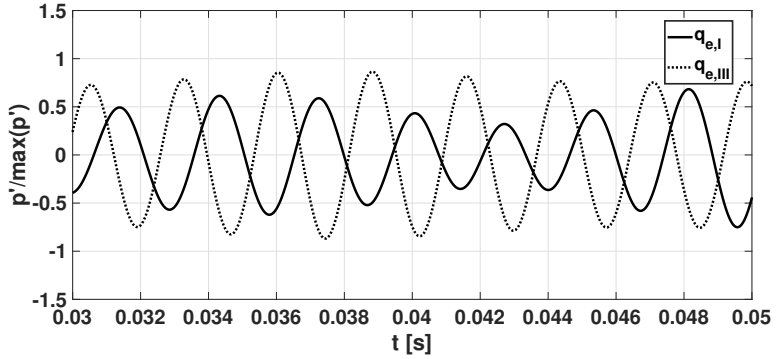

FIGURE 16 Normalized pressure signals of the turbulent jet flame obtained considering the source termes $q_{e,I}$ and $q_{e,III}$ filtered to include only frequency components in the range 300Hz $\leq f \leq$ 400Hz [38].

Figure 14 shows the pressure spectra generated by the essential thermoacoustic source terms $q_{e,I}$, $q_{e,h}$, and $q_{e,III}$ discussed in figure 12 . The noise generated by the source term $q_{e,I}$ is dominated by its subsource term $q_{e,h}$, and the entropy noise given by $q_{e,III}$ is slightly higher over most of the frequency range. At the frequencies where the jet flame is excited by the acoustic plenum modes, i.e., $f \approx$ 60Hz, $f \approx$ 360Hz, and $f \approx$ 690Hz, the emission by the entropy noise, i.e., the source term $q_{e,III}$, is clearly higher. Similar to the findings for the generic two-dimensional flames, it is evident that the effect of the entropy source term $q_{e,III}$ must be taken into account for an accurate prediction of the broadband and tonal combustion noise.

With respect to the Rayleigh criterion, the phase relationship between the pressure signals generated by the thermoacoustic source terms $q_{e,I}$ and $q_{e,III}$ is analyzed next. Figure 15 shows the pressure signals generated by each of these two source terms filtered for the low frequency range $f <$ 300Hz. The signals show qualitatively a similar shape. A phase shift between the pressure signals from the two mechanisms is evident. It is of similar magnitude as that in the laminar flames discussed in figure 9 . Figure 16 shows the signals which are filtered such that only the modes in the range 300Hz $< f <$ 400Hz are included. Furthermore, they are normalized by their maximum for a clearer visualization. Again, a phase shift between the signals is evident. Note that both frequency ranges are dominated by acoustic modes from the burner plenum, i.e., at $f \approx$ 60Hz and $f \approx$ 360Hz. Evidently, for the generic two-dimensional laminar flames and the turbulent jet flame the heat release dominated noise generation mechanism, determined by the source term $q_{e,I}$, and entropy inhomogeneity noise generation mechanisms, defined by the source term $q_{e,III}$, respond to an acoustic excitation generating acoustic pressure waves, which are massively, i.e., by $\geq 90°$, phase shifted. The response to the excitation from the inflow perturbation and turbulence is similar in magnitude for both noise generating mechanisms. Although the noisy nature of the broadband signal of the turbulent flame makes a distinct investigation of the phase relationship difficult, the results evidence that the entropy related noise generation mechanism has to be taken into account in the analysis of combustion instabilities for this turbulent jet flame.

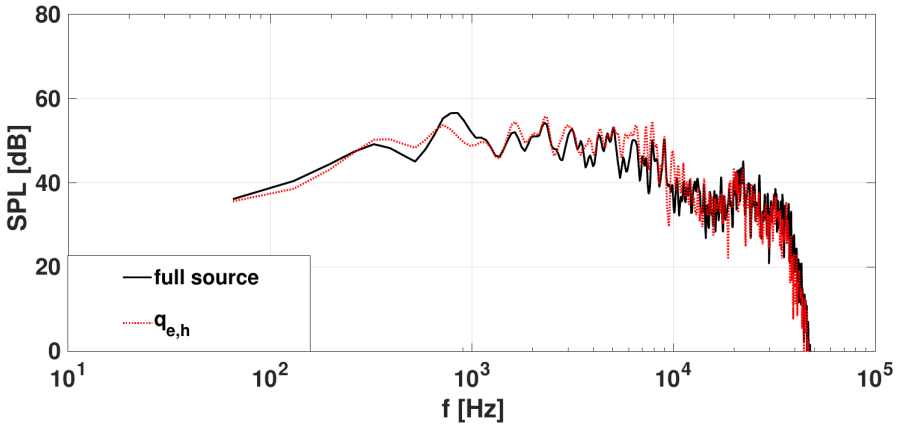

FIGURE 17 The SPL spectra of the unconfined swirl flame for all APE-4 sources (solid black line) and the heat release source $q_{e,h}$ alone (dotted red line) [36].

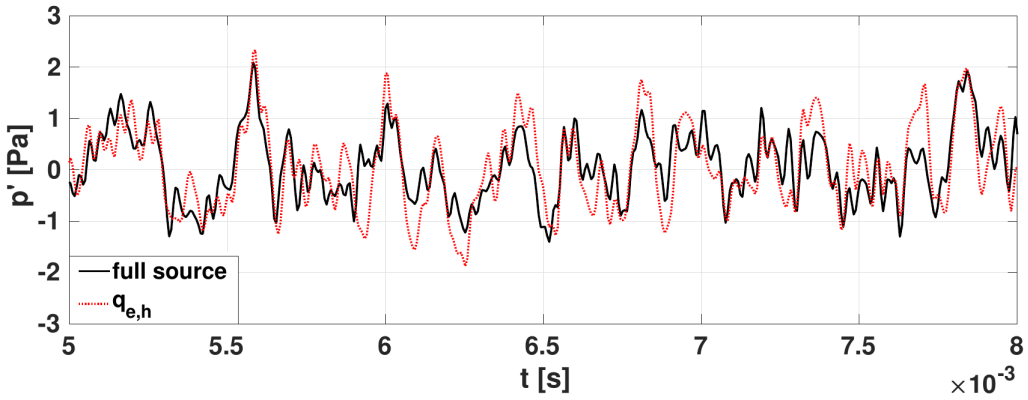

FIGURE 18 Pressure signal of the unconfined burner for all APE-4 sources (solid black line) and the heat release source $q_{e,h}$ alone (dotted red line) [36].

4.3 | Acoustic source analysis of swirl flames

In the following, the noise sources of swirl flames are analyzed. That is, an unconfined and a confined swirl flame is considered to evaluate the effect of the confinement on the thermoacoustic sources and the acoustic field of the swirl flame. Note that a validation of the computed flow field with experimental data was performed in detail in Herff et al. [21] and a high accuracy of the simulations was evident. The acoustic results of the unconfined swirl burner are discussed first. Thereafter, the analysis is extended to the confined setup.

4.3.1 | Unconfined swirl burner

To show the impact if only the heat release source $q_{e,h}$ is considered, as is often done in thermoacoustic analyses, the SPL spectra of the pressure signals generated by all sources and by the pure heat release source $q_{e,h}$ are comparatively juxtaposed in figure 17 . It is evident that for the current swirl flame the heat release source alone leads to a good approximation of the noise spectrum generated by all sources. Figure 18 shows that the two signals agree well also in time domain. This observation is in agreement with many combustion noise studies, but it differs from the observations in sections 4.1.2 and 4.2 for the laminar and turbulent jet flames, where a reasonably accurate prediction of the acoustic pressure signal could not be achieved by just considering the heat release fluctuations. In figure 19 , the instantaneous flame surface of the unconfined swirl flame and the turbulent jet flame from section 4.2 are comparatively juxtaposed. The swirl burner generates evidently more flame pockets than

(a) (b)

FIGURE 19 Visualization of the instantaneous flame front position by the $c_s = 0.5$ iso-contours colored by the flame front curvature of (a) the unconfined swirl flame and (b) the unconfined jet burner from section 4.2 [36].

the jet burner. The formation and annihilation of these pockets leads to large heat release fluctuations. The global heat release fluctuation relative to the time averaged global heat release of the swirl flame $\dot{Q}'_{rms,swirl}/\overline{\dot{Q}} = 0.079$ is approximately 50% greater than that of the turbulent jet flame $\dot{Q}'_{rms,jet}/\overline{\dot{Q}} = 0.052$. The heat release fluctuations from the formation and annihilation of the flame pockets generate combustion noise [5, 16, 26, 47, 51, 52]. It is conjectured that the fairly good prediction of the pressure signal of the swirl flame just by the heat release fluctuations is related to the massive pocket formation and annihilation. This hypothesis was discussed in further detail in Pausch et al. [36].

4.3.2 | Confined swirl burner

Next, the effect of the confinement on the impact of the acoustic sources on the sound field is analyzed. Figure 20 shows the SPL spectra obtained from CAA simulations on the confined domain. The findings of two simulations are shown. The red line shows the SPL spectrum by the heat release source $q_{e,h}$. Evidently, the heat release fluctuations feed the quarter-wave modes of the combustion chamber, which leads to several peaks in the SPL spectrum. The most energetic corresponds to the quarter-wave mode at $f \approx 670$Hz and the three-quarter wave mode at $f \approx 2000$Hz. Note that the frequency of the quarter-wave mode is higher than the value of 540Hz which was experimentally observed by Moeck et al. [32]. In [32] it was discussed that the measured quarter-wave frequency is significantly lower than the theoretically expected value of 660Hz, and that this is probably due to heat losses in the burnt gases to the burner plate which is not considered in the theory. Since the current numerical study does not take into account heat fluxes at the burner walls, the same explanation holds for the discrepancy between the numerical and experimental data. This also explains the good agreement between the numerical and the theoretical quarter-wave frequency. The comparison in figure 20 of the black line representing the spectrum generated by the full APE-4 source formulation based on the confined LES data and the results based on the pure heat release source reveals, however, that the pure heat release source is not sufficient to predict the amplitude of the limit cycle at $f \approx 670$Hz. This implies that the remaining sources have an impact on the limit-cycle amplitude. Therefore, these sources are analyzed next.

Figure 21 (a) shows the pressure signals of the single most significant sources of the confined setup. That is, the distributions of various source terms are separately illustrated. Unlike for the distributions of the unconfined swirl burner discussed in figures 17 and 18 , the source formulation must comprise the heat release source $q_{e,h}$ together with the entropy source, i.e., the third term $q_{e,III}$ of the energy source given by equation 8, and the momentum subsource $\boldsymbol{q_{m,p}}$ given by equation 5 to accurately reconstruct the signal of the full source formulation. Note that this is the same set of source terms that was needed for an accurate prediction of the pressure signals of the jet flames in sections 4.1.2 and 4.2. However, the impact of these sources on the sound field is different. That is, for the quarter-wave oscillation, which clearly dominates the signal in figure 21 (a), the pressure signals by the various source terms show no significant differences in phase. Thus, for the current flame, the heat release source mispredicts the

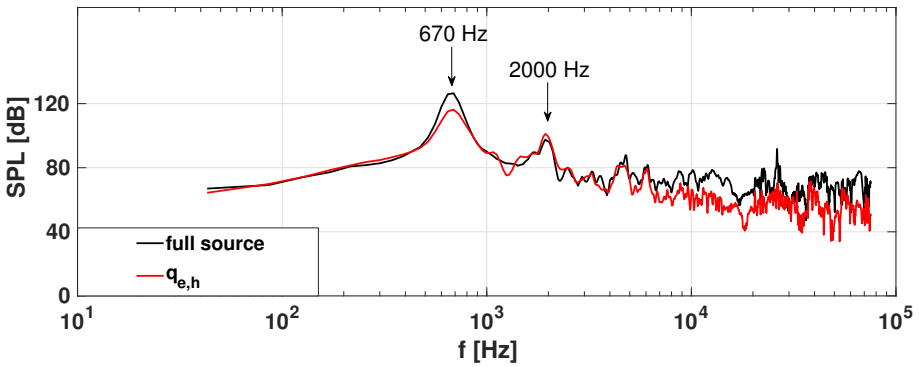

FIGURE 20 SPL spectra of the confined swirl flame by the full APE-4 source formulation (black) and by the pure heat release source $q_{e,h}$ (red). The signals are recorded on the centerline $16D$ downstream of the injector exit [36].

amplitude, but determines the correct phase of the quarter-wave mode oscillation. The term $\boldsymbol{q_{m,p}}$ given in equation 5 amplifies the pressure waves of the quarter-wave mode over the density gradient at the flame front [38]. The source term $q_{e,III}$ is decomposed

$$q_{e,III} = \underbrace{\overline{\boldsymbol{v}} \cdot \left(c^2 \boldsymbol{\nabla}\rho - \boldsymbol{\nabla}p\right)'}_{q_{e,IIIa}} + \underbrace{\boldsymbol{v}' \cdot \overline{\left(c^2 \boldsymbol{\nabla}\rho - \boldsymbol{\nabla}p\right)}}_{q_{e,IIIb}} + \underbrace{\left(\boldsymbol{v}' \cdot \left(c^2 \boldsymbol{\nabla}\rho - \boldsymbol{\nabla}p\right)'\right)'}_{q_{e,IIIc}}, \tag{10}$$

such that the first term $q_{e,IIIa}$ represents the local changes of the flame front position, the second term $q_{e,IIIb}$ is determined by the velocity fluctuations at the mean flame front, and the third term $q_{e,IIIc}$ describes the interaction of the velocity fluctuations and the local flame front. Figure 21 (b) shows that the second mechanism, given by $q_{e,IIIb}$, essentially dominates the emission of $q_{e,III}$ at the quarter-wave mode. That is, the velocity fluctuations induced by the quarter-wave mode at the flame front are a significant source of sound and hence, have an amplifying effect on the burner's limit cycle oscillations. In conclusion, to determine the flow-flame-acoustic interaction of the confined swirl burner configuration not only the heat release $q_{e,h}$ but also the source based on the velocity fluctuations at the mean flame front $q_{e,IIIb}$, and the momentum source $\boldsymbol{q_{m,p}}$ have to be taken into account.

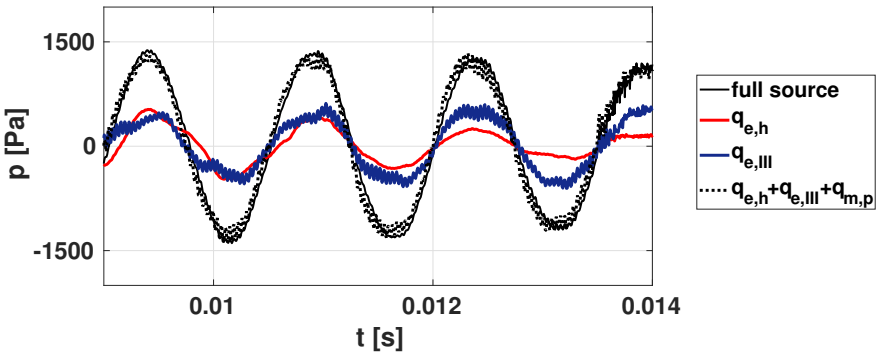

(a)

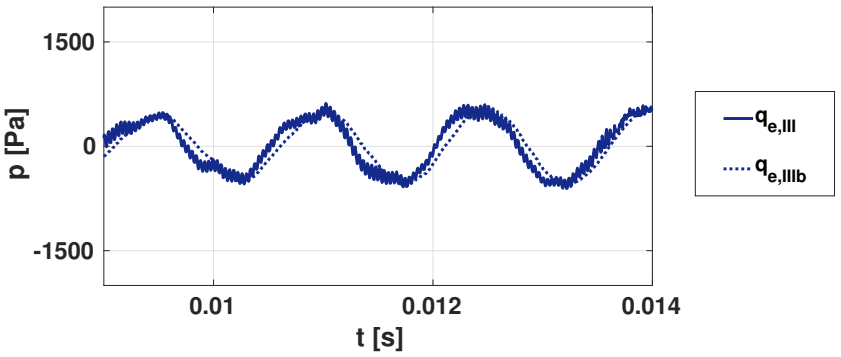

(b)

FIGURE 21 Pressure signal of the confined swirl flame recorded on the centerline $16D$ downstream of the injector exit. (a) shows the signals generated by the full set of sources (solid black line), the heat release source $q_{e,h}$ (solid red), the entropy source $q_{e,III}$, and a reduced set of sources $q_{e,h} + q_{e,III} + \boldsymbol{q_{m,p}}$. (b) shows the signals generated by $q_{e,III} = \left(\boldsymbol{v} \cdot \left(c^2\boldsymbol{\nabla}\rho - \boldsymbol{\nabla}p\right)\right)'$ (solid blue) and by $q_{e,IIIb} = \boldsymbol{v}' \cdot \overline{\left(c^2\boldsymbol{\nabla}\rho - \boldsymbol{\nabla}p\right)}$ (dashed blue) [36].

5 | CONCLUSIONS

The noise source mechanisms of lean-premixed methane-air flames were analyzed using a two-step approach. First, the solutions of the compressible conservation equations for reacting flows were determined by highly resolved large-eddy simulations to compute the acoustic source terms. Second, the sound emissions of different source term considerations were computed by computational aeroacoustics simulations using the acoustic perturbation equations. A good agreement of the pressure signals from the LES and the CAA simulations was shown when all source terms were used for the CAA simulations.

Various flames with increasing complexity were considered. First, the sound mechanisms of harmonically excited generic two-dimensional laminar flames were analyzed. A set of source terms was required to reproduce the overall pressure signals of the laminar flames. These include the effect of the fluctuating heat release rate and the effect of acceleration of entropy gradients. It was shown that the latter is required to predict the correct phase of the pressure signal which is essential to quantify combustion instabilities.

Then, an unconfined turbulent jet flame was investigated. Similar to the results of the harmonically excited laminar flames the sound emission due to the fluctuating heat release and the sound emission due to the acceleration of entropy gradients are phase shifted such that both effects are required to compute the broadband spectrum of the acoustic emission of the turbulent flame.

Finally, the analysis was extended to an unconfined and a confined swirl flame. In contrast to the previously shown results the sound emission of the unconfined swirl flame is dominated by the heat release source alone due to the increased formation and annihilation of flame pockets. In the confined swirl flame configuration a self-excited thermoacoustic instability at the quarter-wave frequency of the burner geometry was found. The phase of this instability was correctly predicted by the heat release source.

However, to accurately compute the limit-cycle amplitude the same set of source terms was required that was also identified to be relevant for the laminar and turbulent jet flames.
The results emphasize that a general simplification of the combustion source mechanisms to only the heat release source is not justified. For the discussed flames only the sound emission of the unconfined swirl flame was accurately predicted while neglecting all other sources of sound. Consequently, it is concluded that the prediction of combustion instabilities requires a cautious choice of the considered acoustic source terms.

ACKNOWLEDGMENTS

The authors explicitly thank Daniel Durox from the Laboratoire EM2C, CNRS, CentraleSupelec for providing the detailed geometry data of the swirl burner. This study was funded by the Deutsche Forschungsgemeinschaft (DFG, German Research Foundation) – GZ: SCHR 309/70-1, AOBJ: 639366. The authors are grateful for the computing resources provided by the High Performance Computing Center Stuttgart (HLRS) within a Large-Scale Project of the Gauss Center for Supercomputing (GCS).

Financial disclosure

None reported.

Conflict of interest

The authors declare no potential conflict of interests.

References

[1] F. Bake et al., *The entropy wave generator (ewg): a reference case on entropy noise*, J. Sound Vib. **326** (2009), no. 3, 574–598.

[2] S. Bomberg, T. Emmert, and W. Polifke, *Thermal versus acoustic response of velocity sensitive premixed flames*, Proc. Combust. Inst. **35** (2015), 3185–3192.

[3] J. Boris et al., *New insights into large eddy simulation*, Fluid Dyn. Res. **10** (1992), no. 4, 199 – 228.

[4] J.-F. Bourgouin et al., *Sensitivity of swirling flows to small changes in the swirler geometry*, C. R. Mécanique **341** (2013), no. 1-2, 211–219.

[5] D. Brouzet et al., *Annihilation events topology and their generated sound in turbulent premixed flames*, Combust. Flame **204** (2019), 268–277.

[6] T. P. Bui, W. Schröder, and M. Meinke, *Numerical analysis of the acoustic field of reacting flows via acoustic perturbation equations*, Comp. Fluids **37** (2008), 1157–1169.

[7] T. P. Bui et al., *Analysis of different sound source formulations to simulate combustion generated noise using a hybrid LES/APE-RF method*, Int. J. Aeroacoustics **8** (2009), 95–124.

[8] D. Crighton et al., *Modern methods in analytical acoustics*, Springer-Verlag Berlin Heidelberg, 1992.

[9] A. P. Dowling and S. Stow, *Acoustic analysis of gas turbine combustors*, J. Propul. Power **19** (2003), 751–764.

[10] F. Duchaine et al., *Sensitivity analysis of transfer functions of laminar flames*, Combust. Flame **158** (2011), no. 12, 2384–2394.

[11] S. Ducruix, D. Durox, and S. Candel, *Theoretical and experimental determinations of the transfer function of a laminar premixed flame*, Proc. Combust. Inst. **28** (2000), no. 1, 765–773.

[12] R. Ewert and W. Schröder, *Acoustic perturbation equations based on flow decomposition via source filtering*, J. Comput. Phys. **188** (2003), 365–398.

[13] M. Fleifil et al., *Response of a laminar premixed flame to flow oscillations: A kinematic model and thermoacoustic instability results*, Combust. Flame **106** (1996), no. 4, 487–510.

[14] G. Geiser, D. Marinc, and W. Schröder, *Comparison of source reconstruction methods for hybrid aeroacoustic predictions*, Int. J. Aeroacoust **12** (2013), no. 7-8, 639–662.

[15] G. Geiser et al., *Thermoacoustics of a turbulent premixed flame*, AIAA Paper 2014-2476 (2014).

[16] A. Haghiri et al., *Sound generation by turbulent premixed flames*, J. Fluid. Mech. **843** (2018), 29–52.

[17] D. Hartmann, M. Meinke, and W. Schröder, *An adaptive multilevel multigrid formulation for cartesian hierarchical grid methods*, Comp. Fluids **37** (2008), 1103–1125.

[18] D. Hartmann, M. Meinke, and W. Schröder, *The constrained reinitialization equation for level set methods*, J. Comput. Phys. **229** (2010), 1514–1535.

[19] D. Hartmann, M. Meinke, and W. Schröder, *A level-set based adaptive-grid method for premixed combustion*, Combust. Flame **158** (2011), no. 7, 1318–1339.

[20] S. Herff et al., *Impact of burner plenum acoustics on the sound emission of a turbulent lean premixed open flame*, Int. J. Spray Combust. **12** (2020), no. 1, 1–20.

[21] S. Herff et al., *LES of a turbulent swirl flame using a mesh adaptive level-set method with dynamic load balancing*, Comput. Fluids **221** (2021), 104900.

[22] M. Hoeijmakers et al., *Intrinsic instability of flame-acoustic coupling*, Combust. Flame **161** (2014), 2860–2867.

[23] F. Hu, M. Hussaini, and J. Manthey, *Low-dissipation and low-dispersion runge-kutta schemes for computational acoustics*, J. Comput. Phys. **124** (1996), 177–197.

[24] M. Ihme, *Combustion and engine-core noise*, Annu. Rev. Fluid Mech. **49** (2017), no. 1, 277–310.

[25] S. Johansson, *High order finite difference operators with the summation by parts property based on DRP schemes,* Technical Report 2004-035, Uppsala University, Department of Scientific Computing, 2004.

[26] N. Karimi et al., *Linear and non-linear forced response of a conical, ducted, laminar premixed flame*, Combust. Flame **156** (2009), no. 11, 2201–2212.

[27] J. J. Keller, *Thermoacoustic oscillations in combustion chambers of gas turbines*, AIAA J. **33** (1995), no. 12, 2280–2287.

[28] C. Kraus, L. Selle, and T. Poinsot, *Coupling heat transfer and large eddy simulation for combustion instability prediction in a swirl burner*, Combust. Flame **191** (2018), 239–251.

[29] T. Lieuwen and V. Yang, *Combustion Instabilities in Gas Turbine Engines: Operational Experience, Fundamental Mechanisms, and Modeling. Progress in Aeronautics and Astronautics series*, vol. 210, AIAA, Reston, VA, 2005.

[30] F. Marble and S. Candel, *Acoustic disturbance from gas non-uniformities convected through a nozzle*, J. Sound Vib. **55** (1977), 225–243.

[31] D. Mejia et al., *Wall-temperature effects on flame response to acoustic oscillations*, Proc. Combust. Inst. **35** (2015), no. 3, 3201–3208.

[32] J. P. Moeck et al., *Nonlinear interaction between a precessing vortex core and acoustic oscillations in a turbulent swirling flame*, Combust. Flame **159** (2012), no. 8, 2650–2668.

[33] V. Moureau, B. Fiorina, and H. Pitsch, *A level set formulation for premixed combustion LES considering the turbulent flame structure*, Combust. Flame **156** (2009), no. 4, 801–812.

[34] U. Müller, M. Bollig, and N. Peters, *Approximations for burning velocities and markstein numbers for lean hydrocarbon and methanol flames*, Combust. Flame **108** (1997), 349–356.

[35] H. Nawroth and C. O. Paschereit, *High-speed flow field measurements of turbulent jet flames undergoing shear layer manipulation*, AIAA Paper 2016-1841 (2016).

[36] K. Pausch, S. Herff, and W. Schröder, *Noise sources of an unconfined and a confined swirl burner*, J. Sound. Vib. **475** (2020), no. 9, 115293.

[37] K. Pausch et al., *Noise sources of a lean-premixed jet flame*, AIAA Paper 2018-4088 (2018).

[38] K. Pausch et al., *Noise sources of lean premixed flames*, Flow Turbul. Combust. **103** (2019), no. 3, 773–796.

[39] T. Poinsot, *Prediction and control of combustion instabilities in real engines*, Proc. Combust. Inst. **36** (2017), no. 1, 1–28.

[40] T. Poinsot and S. Lele, *Boundary conditions for direct simulations of compressible viscous flows*, J. Comput. Phys. **101** (1992), 104–129.

[41] R. Rajaram and T. Lieuwen, *Acoustic radiation from turbulent premixed flames*, J. Fluid Mech. **637** (2009), 357–385.

[42] L. Rayleigh, *The explanation of certain acoustical phenomena*, Nature **18** (1878), 319–321.

[43] S. Schlimpert et al., *Hydrodynamic instability and shear layer effects in turbulent premixed combustion*, Phys. Fluids **28** (2016), no. 1.

[44] S. Schlimpert et al., *Analysis of combustion noise of a turbulent premixed slot jet flame*, Combust. Flame **175** (2017), no. 1, 292–306.

[45] L. Schneiders et al., *An accurate moving boundary formulation in cut-cell methods*, J. Comput. Phys. **235** (2013), 786–809.

[46] L. Schneiders et al., *An efficient conservative cut-cell method for rigid bodies interacting with viscous compressible flows*, J. Comput. Phys. **311** (2016), 62–68.

[47] T. Schuller, D. Durox, and S. Candel, *Self-induced combustion oscillations of laminar premixed flames stabilized on annular burners*, Comb. and Flame **135** (2003), no. 4, 525–537.

[48] T. Schuller, D. Durox, and S. Candel, *A unified model for the prediction of laminar flame transfer functions: comparisons between conical and v-flame dynamics*, Combust. Flame **134** (2003), no. 1–2, 21–34.

[49] W. Strahle, *A review of combustion generated noise*, AIAA Paper 73-1023 (1973).

[50] L. Strobio Chen, S. Bomberg, and W. Polifke, *Propagation and generation of acoustic and entropy waves across a moving flame front*, Combust. Flame **166** (2016), 170–180.

[51] M. Talei, M. J. Brear, and E. R. Hawkes, *Sound generation by laminar premixed flame annihilation*, J. Fluid Mech. **679** (2011), 194–218.

[52] M. Talei, M. J. Brear, and E. R. Hawkes, *A parametric study of sound generation by premixed laminar flame annihilation*, Combust. Flame **159** (2012), 757–769.

[53] C. K. W. Tam and J. C. Webb, *Dispersion-relation-preserving finite difference schemes for computational acoustics*, J. Comput. Phys. **107** (1993), 262–281.

[54] F. Zhang et al., *Effect of unsteady stretching on the flame local dynamics*, Combust. Flame **175** (2017), 170–179.